



**CHALMERS**  
UNIVERSITY OF TECHNOLOGY

## **Suppressing Co-Crystallization of Halogenated Non-Fullerene Acceptors for Thermally Stable Ternary Solar Cells**

Downloaded from: <https://research.chalmers.se>, 2024-04-24 15:55 UTC

Citation for the original published paper (version of record):

Hultmark, S., Paleti, S., Harillo, A. et al (2020). Suppressing Co-Crystallization of Halogenated Non-Fullerene Acceptors for Thermally Stable Ternary Solar Cells. *Advanced Functional Materials*, 30(48).  
<http://dx.doi.org/10.1002/adfm.202005462>

N.B. When citing this work, cite the original published paper.

# Suppressing Co-Crystallization of Halogenated Non-Fullerene Acceptors for Thermally Stable Ternary Solar Cells

Sandra Hultmark, Sri Harish Kumar Paleti, Albert Harillo, Sara Marina, Ferry Anggoro Ardy Nugroho, Yanfeng Liu, Leif K. E. Ericsson, Ruipeng Li, Jaime Martín, Jonas Bergqvist, Christoph Langhammer, Fengling Zhang, Liyang Yu, Mariano Campoy-Quiles, Ellen Moons, Derya Baran,\* and Christian Müller\*

While photovoltaic blends based on non-fullerene acceptors are touted for their thermal stability, this type of acceptor tends to crystallize, which can result in a gradual decrease in photovoltaic performance and affects the reproducibility of the devices. Two halogenated indacenodithienothiophene-based acceptors that readily co-crystallize upon mixing are studied, which indicates that the use of an acceptor mixture alone does not guarantee the formation of a disordered mixture. The addition of the donor polymer to the acceptor mixture readily suppresses the crystallization, which results in a fine-grained ternary blend with nanometer-sized domains that do not coarsen due to a high  $T_g \approx 200^\circ\text{C}$ . As a result, annealing at temperatures of up to  $170^\circ\text{C}$  does not markedly affect the photovoltaic performance of ternary devices, in contrast to binary devices that suffer from acceptor crystallization in the active layer. The results indicate that the ternary approach enables the use of high-temperature processing protocols, which are needed for upscaling and high-throughput fabrication of organic solar cells. Further, ternary devices display a stable photovoltaic performance at  $130^\circ\text{C}$  for at least 205 h, which indicates that the use of acceptor mixtures allows to fabricate devices with excellent thermal stability.

## 1. Introduction

The state-of-the-art power conversion efficiency (PCE) of lab-scale solution-processed organic solar cells is approaching 18%.<sup>[1,2]</sup> The translation of these record values to large-area modules as well as long-term stability are prerequisites for commercialization. A considerable amount of work has been done to address stability issues related to the device electrodes and interlayers.<sup>[3,4]</sup> The stability of the bulk-heterojunction active layer, however, requires further development. Bulk heterojunctions are blends of donor and acceptor materials with an intricate nanostructure that provides both efficient charge generation and transport.<sup>[5–7]</sup> Typically, the optimal blend nanostructure is far away from thermal equilibrium and hence tends to change with time, for example, through phase separation or crystallization, which results in a gradual

S. Hultmark, Prof. C. Müller  
Department of Chemistry and Chemical Engineering  
Chalmers University of Technology  
Göteborg 41296, Sweden  
E-mail: christian.muller@chalmers.se

S. H. K. Paleti, Prof. D. Baran  
King Abdullah University of Science and Technology (KAUST)  
Division of Physical Sciences and Engineering and KAUST  
Solar Center (KSC)  
Thuwal 23955-6900, Saudi Arabia  
E-mail: derya.baran@kaust.edu.sa  
A. Harillo, Dr. M. Campoy-Quiles  
Institut de Ciència de Materials de Barcelona (ICMAB-CSIC)  
Campus de la UAB  
Bellaterra 08193, Spain

 The ORCID identification number(s) for the author(s) of this article can be found under <https://doi.org/10.1002/adfm.202005462>.

© 2020 The Authors. Published by Wiley-VCH GmbH. This is an open access article under the terms of the Creative Commons Attribution License, which permits use, distribution and reproduction in any medium, provided the original work is properly cited.

DOI: 10.1002/adfm.202005462

S. Marina, Dr. J. Martín  
POLYMAT and Polymer Science and Technology Department  
Faculty of Chemistry  
University of the Basque Country UPV/EHU  
Paseo Manuel de Lardizabal 3, Donostia-San Sebastián 20018, Spain

S. Marina, Dr. J. Martín  
Ikerbasque Basque Foundation for Science  
Bilbao 48013, Spain

Dr. F. A. A. Nugroho, Prof. C. Langhammer  
Department of Physics  
Chalmers University of Technology  
Göteborg 41296, Sweden

Y. Liu, Dr. J. Bergqvist, Prof. F. Zhang  
Department of Physics  
Chemistry and Biology (IFM)  
Linköping University  
Linköping 58183, Sweden

Dr. L. K. E. Ericsson, Prof. E. Moons  
Department of Engineering and Physics  
Karlstad University  
Karlstad 65188, Sweden

Dr. R. Li  
National Synchrotron Light Source II  
Brookhaven National Laboratory  
New York, NY 11973, USA

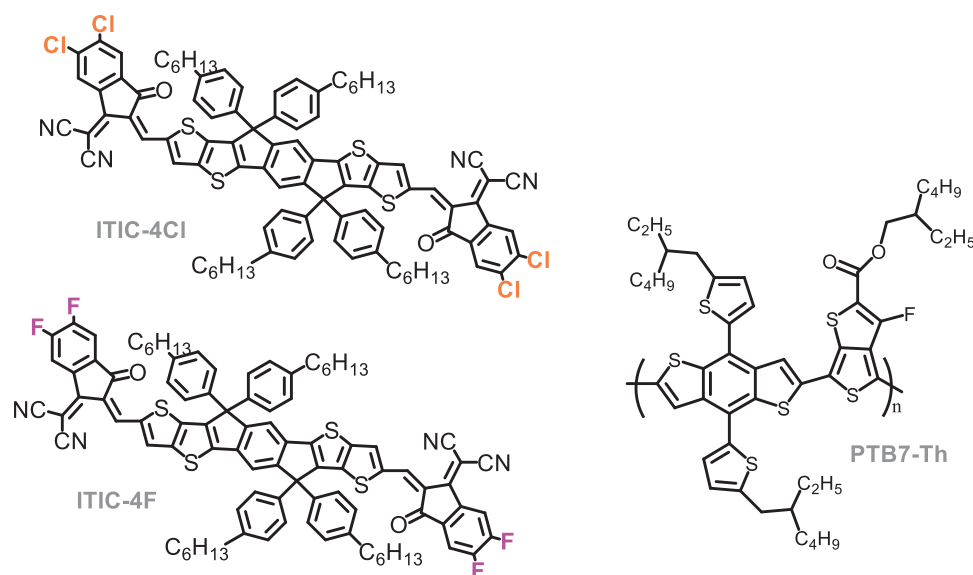


**Figure 1.** Chemical structures of ITIC-4Cl, ITIC-4F and PTB7-Th.

decrease in photovoltaic performance. Many blends are finely mixed and display a single glass transition temperature  $T_g$ , which represents an upper limit above which the nanostructure rapidly coarsens.<sup>[8]</sup>

Current understanding of structure–property relationships related to the thermal stability of bulk-heterojunction blends is based on the large body of work on fullerene-based solar cells. Fullerene crystals rapidly form upon heating above the blend  $T_g$  and disrupt the nanostructure of the active layer.<sup>[9,10]</sup> One widely explored strategy to suppress crystallization of the fullerene acceptor involves the use of fullerene mixtures.<sup>[11–13]</sup>

The superior thermal stability of fullerene mixtures arises due to the increase in entropy upon mixing by  $\Delta S_{\text{mix}} = -Nk_B \sum_i \phi_i \ln \phi_i$ , where  $N$  is the number of molecules,  $k_B$  the Boltzmann constant, and  $\phi_i$  the molar fraction of component  $i$ .<sup>[14]</sup> The resulting decrease in the Gibbs free energy of the liquid state, that is, the disordered mixture of several acceptor molecules, reduces the tendency for crystallization. As a result, mixing of several components tends to impede coarsening of the multicomponent (i.e., ternary, quaternary, etc.) blend.

The best performing solar cells are now consistently realized with non-fullerene acceptors, which offer additional advantages over fullerenes such as more cost-effective synthesis, stronger optical absorption, and a higher degree of chemical stability.<sup>[15–17]</sup> Non-fullerene acceptors such as the acceptor 3,9-bis(2-methylene-(3-(1,1-dicyanomethylene)-indanone))-5,5,11,11-tetrakis(4-hexylphenyl)-dithieno[2,3-d:2',3'-d']-s-indaceno[1,2-b:5,6-b']dithiophene (ITIC) and its many derivatives readily crystallize upon annealing, and hence create a rich blend nanostructure that can only be controlled by complex processing schemes.<sup>[18,19]</sup> Crystal

nucleation of ITIC occurs at temperatures as low as 100 °C despite a very high  $T_g \approx 180$  °C, giving rise to nanometer-sized crystallites whose number and size strongly depend on the precise annealing time and temperature.<sup>[20]</sup> Further, ITIC derivatives can form several different polymorphs, which further complicates their phase behavior.<sup>[20–23]</sup> The range of temperatures where non-fullerene crystals are prone to form covers the processing conditions that are commonly selected for the roll-to-roll fabrication of organic solar cells. For instance, printing on flexible poly(ethylene terephthalate) (PET) foil is typically done at temperatures up to 140 °C, which ensures rapid evaporation of the processing solvent.<sup>[24,25]</sup> Besides, the printing of solution processable hole transport layers requires annealing at similar temperatures.<sup>[26,27]</sup> We argue that considerable gains in terms of device reproducibility could be made if it was possible to process non-fullerene acceptor-based blends at elevated temperatures without the risk of phase separation and acceptor crystallization.<sup>[28]</sup> Attempts to impede the crystallization of non-fullerene acceptors by mixing of several components has met with limited success due to the complex nanostructure of the resulting ternary blends, where the stoichiometry and processing conditions can display either enhanced or suppressed crystallization.<sup>[29]</sup> ITIC derivatives experience stronger attractive forces than fullerenes, caused by  $\pi$ – $\pi$  interactions and, as we will argue below, halogen interactions, which promote crystallization. As a result, mixing of several non-fullerene acceptors, and the associated increase in the entropy of the liquid state  $\Delta S_{\text{mix}}$ , is not a guarantee that crystallization is suppressed.

In this work, we explore the phase behavior of a non-fullerene acceptor binary system based on two ITIC derivatives, ITIC-4F and ITIC-4Cl (see **Figure 1** for chemical structures), which form a complex phase behavior that—in contrast to fullerenes—is governed by both the entropy of mixing as well as positive enthalpic interactions. We find that the two acceptors can co-crystallize, a process which is however suppressed when blended with the benzodithiophene–fluorothienothio-  
phene based donor polymer PTB7-Th (see **Figure 1** for chemical

Dr. L. Yu  
Key Laboratory of Green Chemistry and Technology of Ministry of Education  
College of Chemistry  
Sichuan University  
Chengdu 610064, China

structure). The resulting ternary blend features a fine-grained nanostructure composed of distinct, tens-of-nanometers small domains of the acceptor mixture, intertwined with polymer-rich domains. As a result, the corresponding ternary devices display a stable photovoltaic performance at temperatures approaching the blend  $T_g \approx 200$  °C, in contrast to the corresponding binary ones, which suffer from extensive crystallization of the acceptor considerably below 200 °C.

## 2. Results and Discussion

We study the two acceptors ITIC-4F and ITIC-4Cl (see Figure 1 for chemical structures), motivated by their structural similarity, and the halogenation of the indanone groups that flank the indacenodithienothiophene core on either side. Fluorine has a low polarizability due to its small size as well as a high electronegativity, and hence the  $F \cdots F$  interactions are thought to be weak compared to those of other halogens, such as

$Cl \cdots Cl$  interactions, which are considerably stronger.<sup>[30,31]</sup> In agreement, solution-processed ITIC-4F appears disordered in contrast to ITIC-4Cl whose X-ray diffractogram features sharp diffractions, which indicate a crystalline solid (Figure 2a; Figure S2b, Supporting Information).

Both acceptors display a rich phase behavior. Differential scanning calorimetry (DSC) of ITIC-4F shows a broad endotherm with peak at  $T_{\text{endo}} \approx 155$  °C (Figure 2b,c), above which X-ray diffractions from polymorph  $I_F$  are lost (cf. X-ray diffractogram recorded for material annealed at 160 °C; Figure 2a), indicating that the compound undergoes crystal melting. Above the  $T_g \approx 185$  °C (cf. Figure S1a, Supporting Information) re-crystallization occurs and ITIC-4F forms polymorph  $II_F$ . ITIC-4Cl also displays a  $T_{\text{endo}} \approx 180$  °C, which we assign to a solid–solid phase transformation from polymorph  $I_{Cl}$  to  $II_{Cl}$ , as indicated by distinct differences in the X-ray diffraction patterns recorded at 160 and 200 °C (Figure 2a). Hence, ITIC-4Cl does not undergo re-crystallization above its  $T_g \approx 210$  °C (cf. Figure S1b, Supporting Information), as evidenced by the

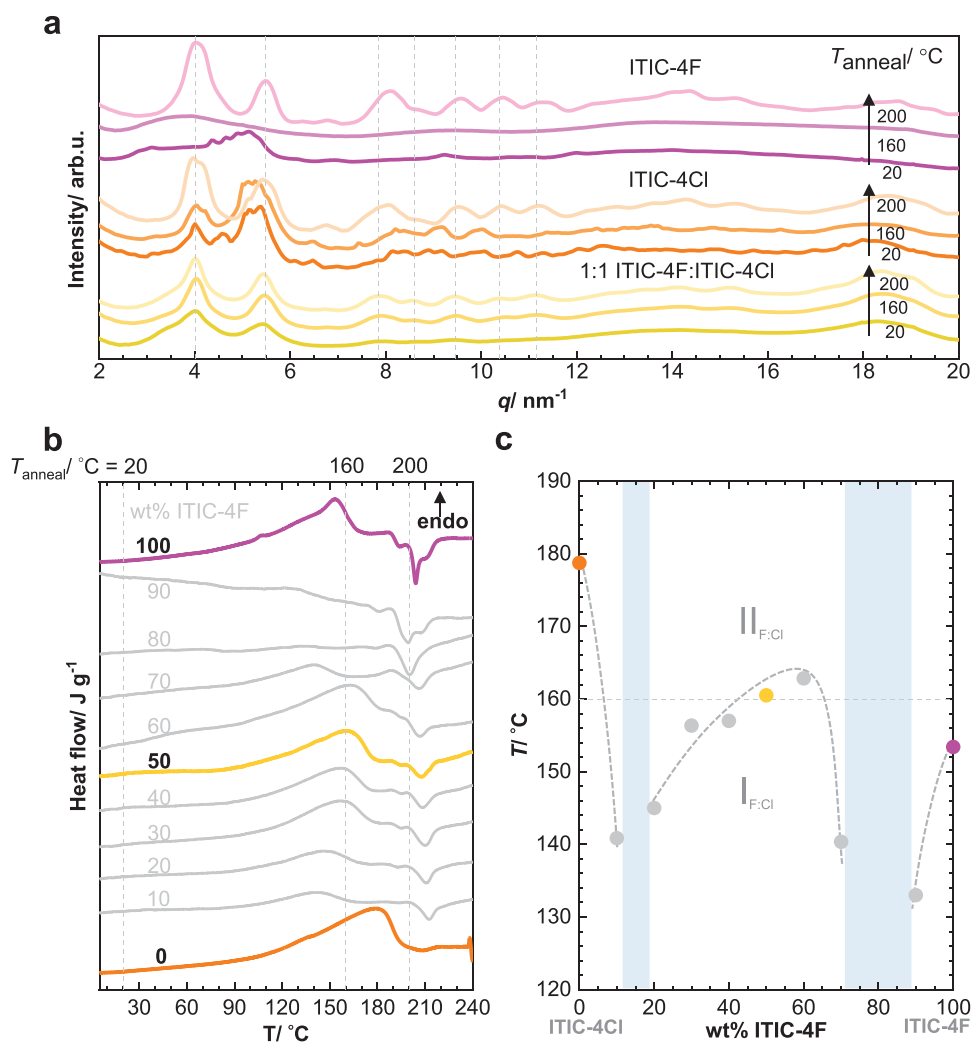


**Figure 2.** a) Radially integrated GIWAXS diffractograms of ITIC-4F, ITIC-4Cl, and 1:1 ITIC-4F:ITIC-4Cl directly after spin-coating, annealing at 160 and 200 °C, dashed lines indicate the peak positions of prominent diffractions observed for 1:1 ITIC-4F:ITIC-4Cl; b) DSC first heating thermograms of ITIC-4F:ITIC-4Cl mixtures; c) Peak temperatures of endothermic transitions corresponding to the solid–solid transition from polymorph  $I_{F:Cl}$  to  $II_{F:Cl}$  (melting of polymorph  $I_F$  in case of ITIC-4F); compositions of mixtures that are mostly disordered are indicated in light blue.

absence of an exotherm above this temperature (Figure 2b). The high temperature polymorphs of both acceptors,  $\text{II}_F$  and  $\text{II}_{Cl}$ , show virtually the same diffraction pattern with distinct peaks at, for example,  $q \approx 4.0$ , 5.5, and  $8.1 \text{ nm}^{-1}$  (Figure 2a; Figure S2b, Supporting Information).

The DSC thermograms of ITIC-4F:ITIC-4Cl binary mixtures display both an endotherm and exotherm, with peak at 160 and  $210^\circ\text{C}$  in case of a 1:1 mixture (Figure 2b). The corresponding GIWAXS diffractogram recorded at  $200^\circ\text{C}$  features distinct crystalline diffractions (Figure 2a), which indicates that the endotherm at  $160^\circ\text{C}$  arises due to a solid–solid state transformation and not crystal melting. We therefore argue that binary mixtures of ITIC-4F and ITIC-4Cl show comparable behavior to ITIC-4Cl, that is, a solid-state transformation from  $\text{I}_{F:Cl}$  to  $\text{II}_{F:Cl}$  (Figure 2c), but followed by an additional crystallization at  $210^\circ\text{C}$ . The X-ray diffraction pattern of  $\text{II}_{F:Cl}$  resembles that of the two neat components, albeit with slightly shifted peaks, which is due to the formation of an acceptor co-crystal. We propose that  $F \cdots Cl$  interactions occur,<sup>[30,31]</sup> which enable incorporation of the two acceptors into the same crystal lattice. Acceptor molecules that have not joined a co-crystal will instead form a homogeneous amorphous mixture, driven by the entropy of mixing  $\Delta S_{\text{mix}}$  as well as, possibly,  $F \cdots Cl$  interactions leading to a decrease in enthalpy upon mixing, that is,  $\Delta H_{\text{mix}} < 0$ . Hence, mixtures of ITIC-4Cl and ITIC-4F are thermodynamically stable and will not undergo liquid–liquid phase separation below  $200^\circ\text{C}$ .

We went on to study the phase behavior of the ITIC-4F:ITIC-4Cl mixture when blended with the donor polymer PTB7-Th. We focus on a blend ratio of 1:0.5:0.5 (wt%) PTB7-Th:ITIC-4F:ITIC-4Cl, which also offers the best photovoltaic performance (cf. discussion on device performance below).

Diffraction patterns of the as-cast ternary blend, as well as films annealed at  $160^\circ\text{C}$  only feature a broad amorphous halo around  $q \approx 17 \text{ nm}^{-1}$  (Figure S2a,b, Supporting Information), which suggests that the presence of the polymer effectively suppresses crystallization of the acceptor mixture (note that PTB7-Th does not crystallize; cf. Figure S2a,b, Supporting Information, and ref. [32]). Annealing at  $200^\circ\text{C}$  ultimately results in crystallization of the acceptor mixture, as evidenced by the appearance of distinct diffraction peaks as well as an exotherm in DSC heating thermograms (cf. Figures S2a and S3, Supporting Information).

Since crystallization of the acceptor mixture in the ternary blend only occurs above  $200^\circ\text{C}$ , we suspected that the ternary blend displays a  $T_g$  at a similar temperature. We performed physical aging experiments of the ternary blend using fast scanning calorimetry (FSC) to determine its  $T_g$ . First, we heated a thin film of the ternary blend to  $450^\circ\text{C}$  to delete the thermal history, followed by annealing (aging) at different temperatures for 30 min. Quenching from  $450$  to  $-90^\circ\text{C}$  gave a reference scan void of crystallization (see the heating thermogram in Figure 3a). Reorganization of molecules to a more equilibrated thermodynamic state takes place below the  $T_g$  if given enough time. This reorganization results in an endothermic overshoot in a subsequent FSC heating scan. The enthalpy overshoot decreases in magnitude and shifts to higher temperatures as the aging temperature approaches the  $T_g$  (Figure 3b), and hence the aging temperature where the enthalpy change  $\Delta H$  goes to zero is a measure for the  $T_g$ .<sup>[33]</sup> We obtain a value of  $T_g \approx 205^\circ\text{C}$  for the ternary blend, and  $195$  and  $215^\circ\text{C}$  for the two binaries PTB7-Th:ITIC-4F and PTB7-Th:ITIC-4Cl, respectively (Figure 3b; Figure S4, Supporting Information). The midpoint of the corresponding step in FSC heating scans indicates

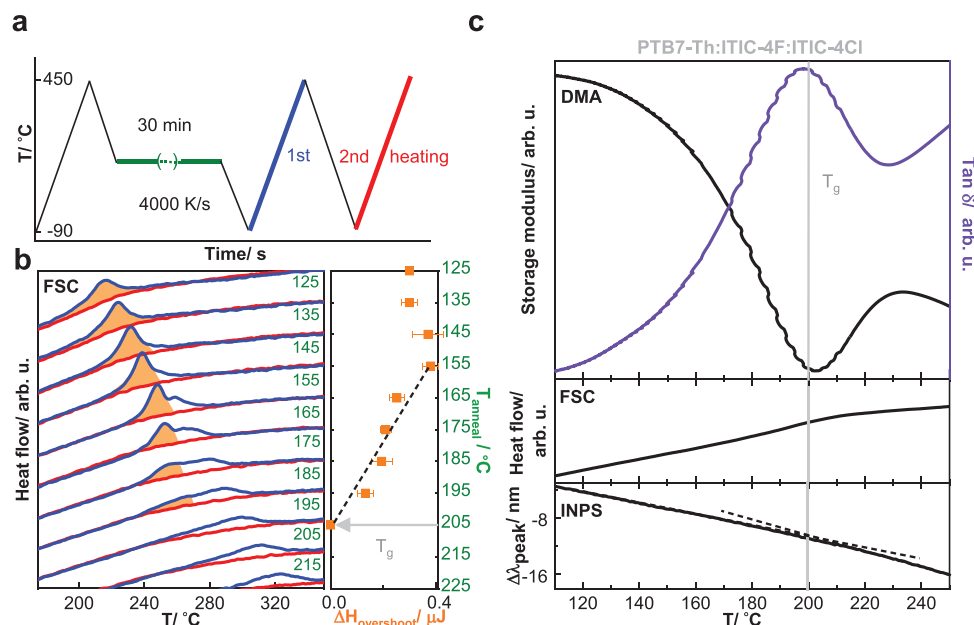


**Figure 3.** a) FSC protocol: the sample is first rapidly heated to  $450^\circ\text{C}$  and then annealed for 30 min at different annealing temperatures  $T_{\text{anneal}}$  (green), followed by a first (blue) and second heating scan (red), both after quenching to  $-90^\circ\text{C}$ ; b) FSC heating thermograms of the 1:0.5:0.5 PTB7-Th:ITIC-4F:ITIC-4Cl ternary blend after annealing (blue) and after quenching from  $450$  to  $-90^\circ\text{C}$  (red) with the enthalpy overshoot indicated in orange (left); the temperature where the enthalpy overshoot  $\Delta H_{\text{overshoot}}$  approaches zero corresponds to the  $T_g$  (right); c) DMA thermogram showing the storage modulus and loss tangent  $\tan \delta$ , FSC heating thermogram recorded after quenching the sample, and plasmonic nanospectroscopy, or indirect nanoplasmonic sensing (INPS), of the ternary blend showing the relative shift of the localized surface plasmon resonance peak  $\Delta\lambda_{\text{peak}}$  with temperature.



similar values of 200, 190, and 212 °C for the ternary and the two binary blends, respectively. We were able to confirm the  $T_g$  values with dynamic mechanical analysis (DMA), and plasmonic nanospectroscopy (Figure 3c; Table S1, Figure S5, Supporting Information).<sup>[34,35]</sup> Notably, for the ternary blend, the loss tangent  $\tan \delta$  from DMA first heating thermograms peaks at 200 °C, and the shift of the plasmonic resonance peak  $\Delta\lambda_{\text{peak}}$  changes slope at the same temperature, which is in good agreement with our FSC data (Figure 3c).

In a further set of experiments, we compared the tendency of the acceptor to crystallize in binary and ternary blends. Samples were annealed at  $T_{\text{anneal}} = 160$  °C for 10 min and 24 h, respectively. The typical crystal size is on the order of a few hundred

nanometers, which we explain with diffusion-limited crystallization below the  $T_g$ , similar to the crystallization behavior of ITIC.<sup>[20]</sup> Acceptor crystals are clearly visible in optical micrographs and scanning electron microscopy (SEM) images of both binary blends after 10 min (Figure 4b; Figure S6, Supporting Information). After 24 h, the crystallites visible in the binary blends have grown in size (Figure S7, Supporting Information). In contrast, no crystals can be observed in the case of the ternary blend at 160 °C after 10 min or 24 h, which indicates that the ternary blend is more thermally stable (Figure 4b).

We used atomic force microscopy based infrared spectroscopy (AFM-IR) to elucidate the make-up of the blend nanostructure in more detail. First, we used AFM-IR to confirm that

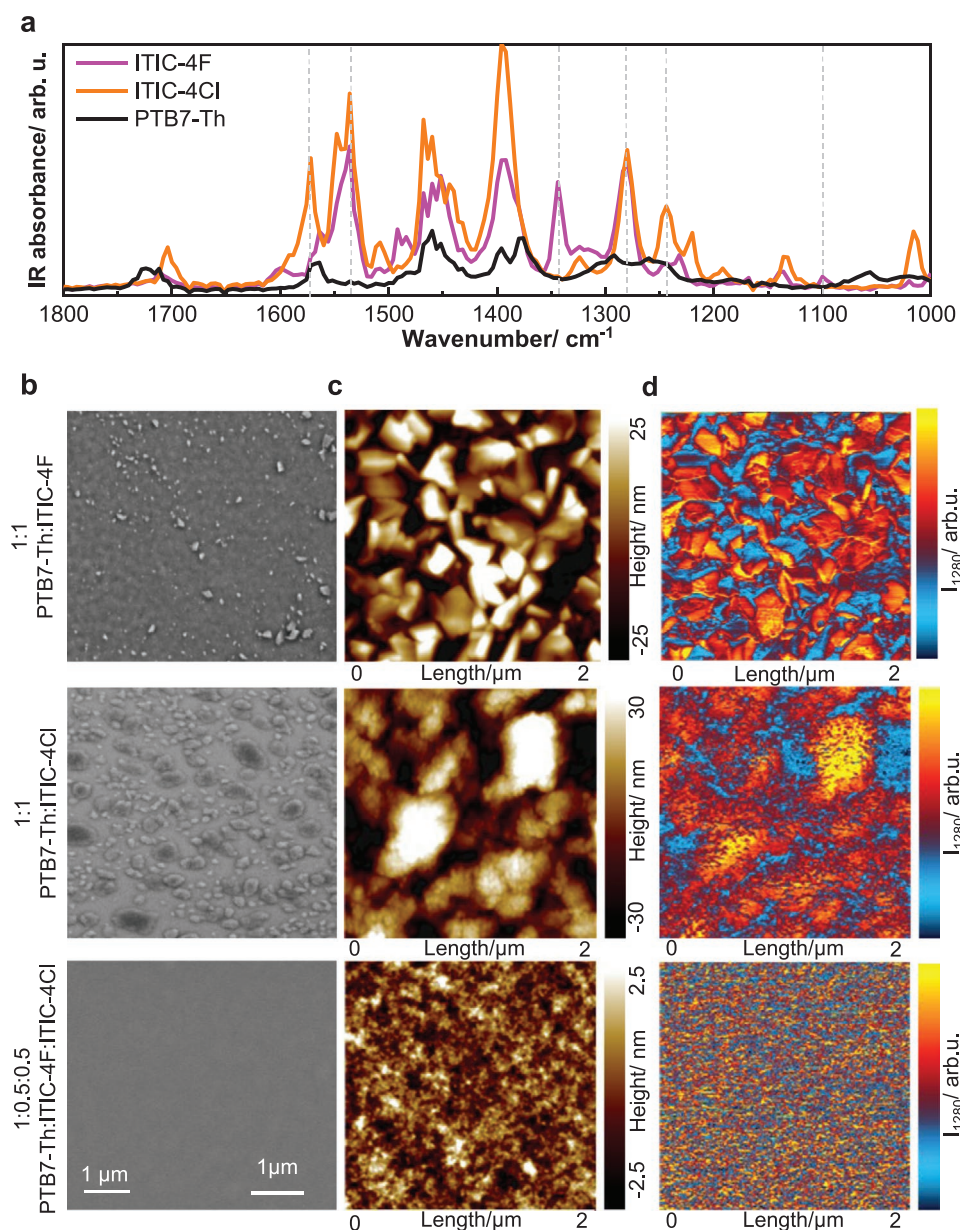


**Figure 4.** a) AFM-IR spectra recorded for neat films of PTB7-Th, ITIC-4F, and ITIC-4Cl with a resolution of 4 cm<sup>-1</sup> per pt; b) SEM images; c) AFM height images showing the peak-to-valley height difference; and d) AFM-IR images recorded at 1280 cm<sup>-1</sup> of the binary blend 1:1 PTB7-Th:ITIC-4F (top row), PTB7-Th:ITIC-4Cl (center row), and the ternary blend 1:0.5:0.5 PTB7-Th:ITIC-4F:ITIC-4Cl (bottom); all samples annealed at 160 °C for 10 min.

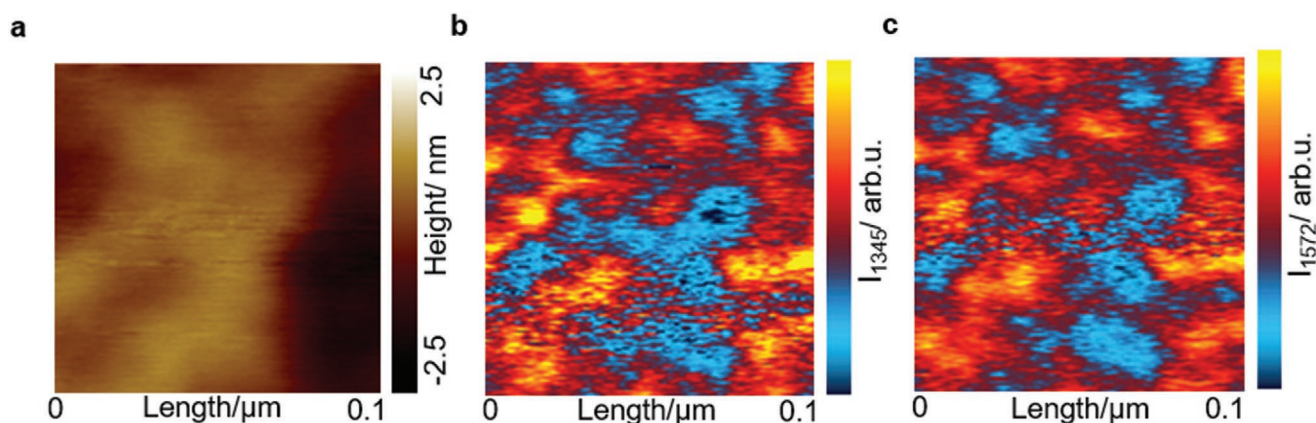


**Figure 5.** The same spot of a 1:0.5:0.5 PTB7-Th:ITIC-4F:ITIC-4Cl ternary film annealed at 160 °C and imaged with a) AFM in height mode; b) AFM-IR recorded at 1345  $\text{cm}^{-1}$ , where only ITIC-4F absorbs; and c) AFM-IR recorded at 1572  $\text{cm}^{-1}$ , where ITIC-4Cl absorbs.

the crystals in thin films of the two binaries consist of ITIC-4F and ITIC-4Cl, respectively. IR spectra recorded at areas covered by crystals are dominated by absorption peaks that arise from the two acceptors, for example, peaks at 1280 and 1540  $\text{cm}^{-1}$  that we assign to stretching vibrations of C–C or  $\text{CH}_2$  twisting and C=C bonds, respectively (Figure 4a). Further, the spectra of both ITIC-4F and ITIC-4Cl show peaks that are unique for each material, that is, peaks at 1345 and 1572  $\text{cm}^{-1}$ , respectively, which we can use to selectively image either material. Mapping of the binary films with AFM-IR or standard AFM in height mode produced images with similar features, that is, those arising from crystals that protrude  $\approx 50\text{--}60$  nm from the film surface and coincide with areas where acceptor specific IR absorption peaks are recorded (Figure 4c,d; Figure S9, Supporting Information). The surface of ternary blend films appears considerably more fine-grained and shows a roughness of only 5 nm. Due to the low surface roughness of ternary blend films we were able to record AFM-IR images at very high magnification. We imaged the same spot in a ternary film annealed at 160 °C with both AFM in height mode (Figure 5a), as well as AFM-IR using an IR-laser wavenumber of 1345  $\text{cm}^{-1}$ , where only ITIC-4F absorbs, or 1572  $\text{cm}^{-1}$ , where ITIC-4Cl absorbs (Figure 5b,c). The two AFM-IR images reveal 10–30 nm small

domains that are similar in shape. We conclude that ITIC-4F and ITIC-4Cl are located in close vicinity to each other and form distinct domains that are uniform in composition, and are intertwined with polymer-rich domains, in agreement with the phase behavior described above (cf. Figure 2c).

We propose that the small size of the ITIC-4F:ITIC-4Cl domains suppresses crystallization of the acceptor mixture due to confinement, that is, nucleation events are rare and hence most of the material is effectively separated from nucleation sites by the surrounding polymer domains. Since the polymer is disordered, and ternary blends display a high degree of photoluminescence (PL) quenching (see discussion below), we argue that the polymer-rich domains nevertheless contain a certain amount of ITIC-4F and ITIC-4Cl, which can be considered as dissolved in the polymer phase. Annealing at 200 °C, that is, at the  $T_g$  of the ternary, results in coarsening as evidenced by somewhat larger domains with a size of 20–50 nm (Figure S8, Supporting Information), as well as co-crystallization of the acceptor mixture (cf. Figure S2a, Supporting Information). Coarsening of the ternary blend at 200 °C and above is corroborated by variable-temperature PL and scattering measurements, which show a clear increase in PL intensity with peak at 820 nm (Figure S10a,b, Supporting Information) and

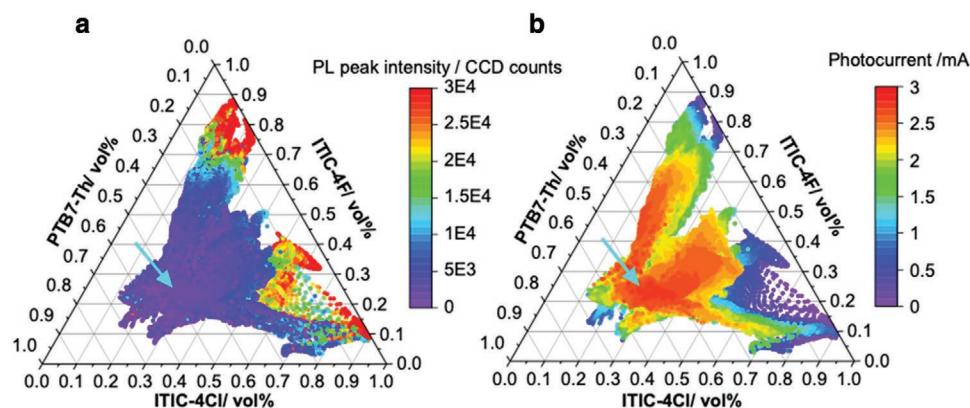


**Figure 6.** Ternary composition diagrams showing a) the photoluminescence intensity, PL; and b) the photocurrent obtained with white light for different compositions of PTB7-Th:ITIC-4F:ITIC-4Cl. The ternary 1:0.5:0.5 PTB7-Th:ITIC-4F:ITIC-4Cl is marked with arrows. The composition in this figure refers to number of molecules per unit volume. We assume that all materials have the same density ( $1 \text{ g cm}^{-3}$ ).

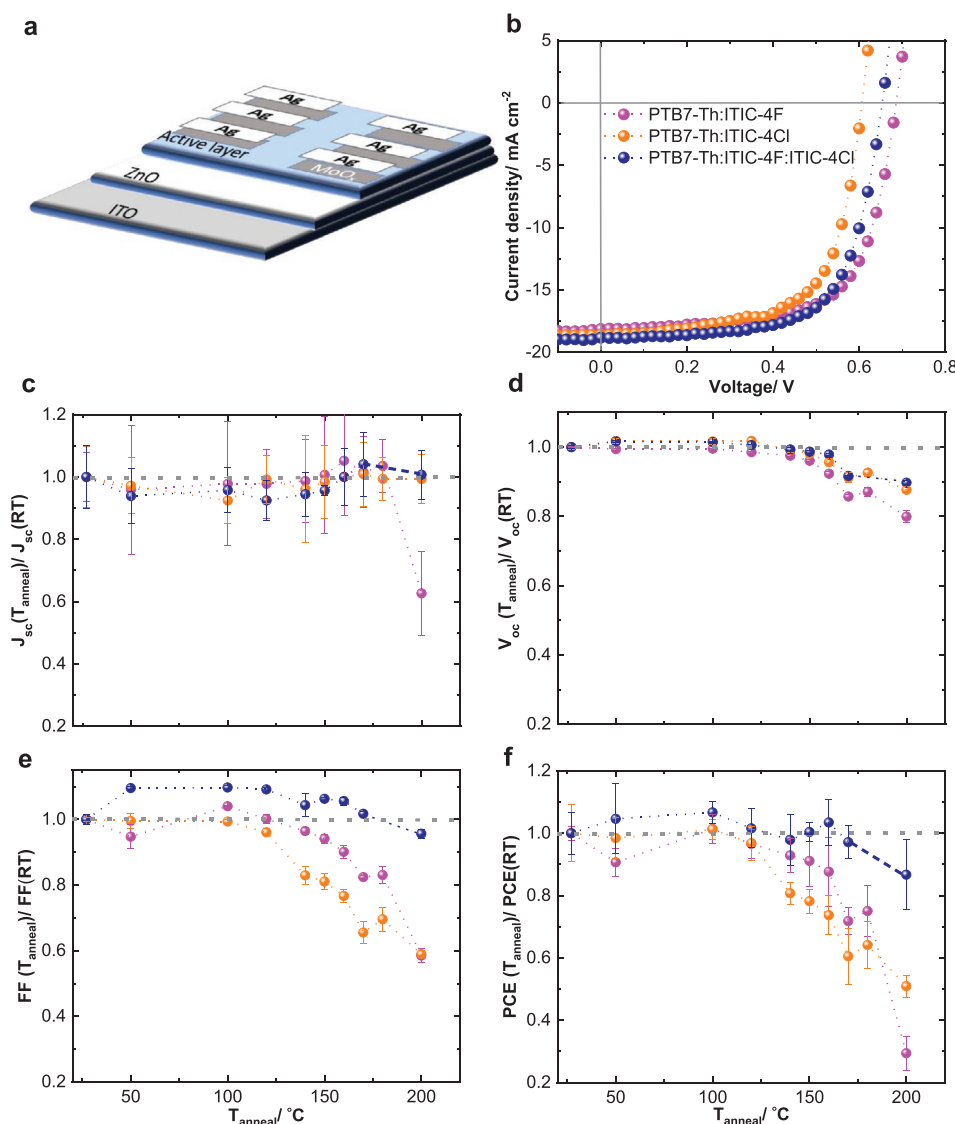


**Figure 7.** a) Photovoltaic device layout, b) Representative current density–voltage ( $J$ – $V$ ) characteristics of devices comprising the two binary blends, 1:1 PTB7-Th:ITIC-4F and 1:1 PTB7-Th:ITIC-4Cl, and the 1:0.5:0.5 PTB7-Th:ITIC-4F:ITIC-4Cl ternary blend, c) Short-circuit current density  $J_{sc}$ , d) Open-circuit voltage  $V_{oc}$ , e) Fill factor  $FF$  and f) Power conversion efficiency  $PCE$  of devices comprising active layers annealed for 10 min at temperatures between 25 and 200 °C; data points represent average values of measurements done for up to 6 pixels on the same substrate.

an increase in scattered laser intensity at 200 °C (Figure S10c, Supporting Information), suggesting that donor and acceptor domains become purer.

To determine the likely range of compositions that will display an optimal photovoltaic performance, we used a combinatorial screening method recently described by Harillo-Banos et al. for ternary solar cells.<sup>[36]</sup> In brief, thin layers of the three components (or mixtures thereof) were sequentially deposited on top of each other, resulting in four samples with different lateral composition gradients that when combined covered approximately 65% of the phase space (see Figure S11, Supporting Information, and Experimental Section for details). We then mapped the local Raman intensity, PL, and photocurrent at all compositions covered by the graded samples to

obtain maps of these parameters (Figure 6; Figure S12, Supporting Information). Analysis of the Raman spectra was used to determine the local composition.<sup>[37]</sup> The PL map indicates the highest degree of PL quenching for compositions that are rich in all three components. We propose that for these compositions the highest degree of intermixing of the donor polymer and acceptor mixture is obtained, in agreement with the AFM-IR based analysis of the ternary blend nanostructure (cf. Figure 5). The photocurrent map shows a similar trend with a broad maximum for compositions ranging from 20–60% PTB7-Th (Figure 6b). We argue that the ternary blend displays a high photovoltaic performance across a wide range of compositions. Therefore, position-dependent deviations from the optimal composition, which would no doubt occur



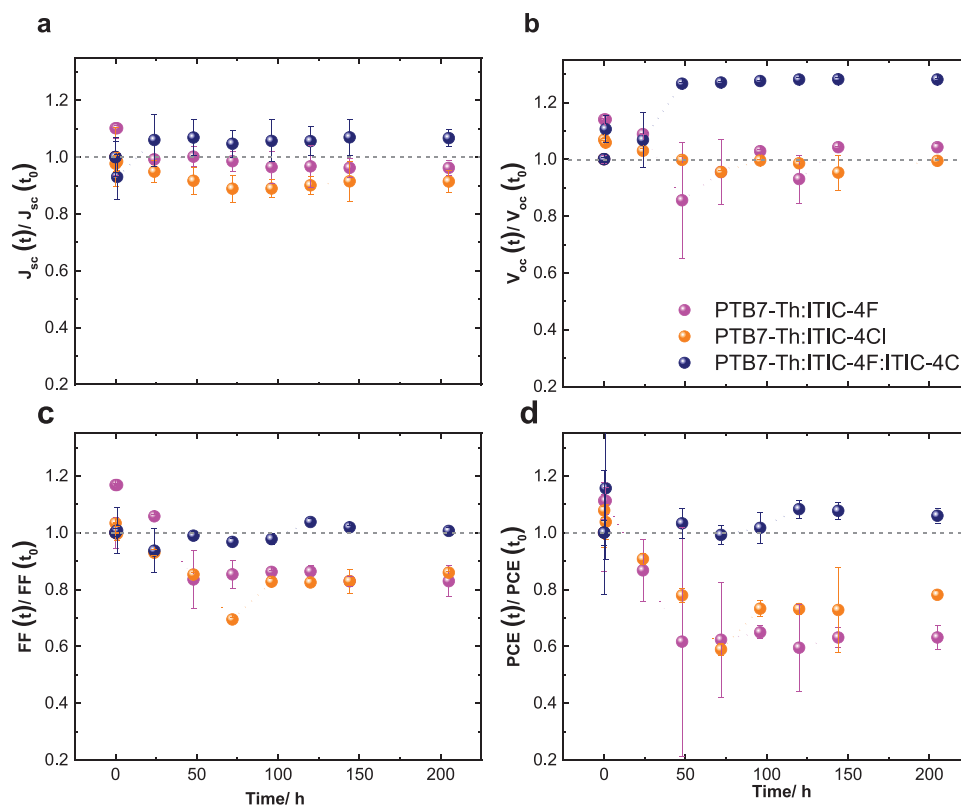


**Figure 8.** a)  $J_{sc}$ , b)  $V_{oc}$ , c) FF, and d) PCE of 1:1 PTB7-Th:ITIC-4F and 1:1 PTB7-Th:ITIC-4Cl binary devices, and 1:0.5:0.5 PTB7-Th:ITIC-4F:ITIC-4Cl ternary devices recorded after annealing for up to 205 h at 130 °C; data points represent average values of measurements done for up to 6 pixels on the same substrate.

if large-area device fabrication was attempted, will nevertheless result in solar cells with limited spatial variation in light harvesting efficiency.

In a further set of experiments, we fabricated a series of solar cells with an inverted architecture and an active layer composed of the ternary blend (see Experimental Section for details). We varied the composition of the active layer blend by changing the ratio of ITIC-4F and ITIC-4Cl, while maintaining a constant 1:1 ratio of donor to acceptor materials (Table S2, Supporting Information). These series of devices covered the range of compositions for which our combinatorial screening experiments had revealed the highest photocurrent (cf. Figure 6a). In agreement with our photocurrent map a ternary blend composition of 1:0.5:0.5 (wt%) PTB7-Th:ITIC-4F:ITIC-4Cl showed the best photovoltaic performance with a short-circuit current density  $J_{sc} \approx 18.6 \text{ mA cm}^{-2}$ , open-circuit voltage  $V_{oc} \approx 660 \text{ mV}$ , and fill factor FF  $\approx 68\%$ , giving rise to a power conversion efficiency PCE  $\approx 8.3\%$  (Table S3, Supporting Information).

We, therefore, studied the thermal stability of the 1:0.5:0.5 ternary devices. We annealed active layers for 10 min at various temperatures up to  $T_{\text{anneal}} = 200 \text{ °C}$  prior to evaporation of the top  $\text{MoO}_x$  interlayer and Ag electrode. For comparison, we also fabricated 1:1 binary blend devices and used the same annealing protocol. Binary blend devices show no drop in  $J_{sc}$  and  $V_{oc}$  up to at least 150 °C (Figure 7c,d). However, we observe a drastic drop in FF by as much as 40% for  $T_{\text{anneal}} > 120 \text{ °C}$ , which we explain by the growth of acceptor crystals that disrupt the blend nanostructure. Overall, annealing of binary blend devices at, for

example,  $T_{\text{anneal}} = 150 \text{ °C}$  results in a drop in PCE by 10% in case of PTB7-Th:ITIC-4F and 20% in case of PTB7-Th:ITIC-4Cl. Ternary blend devices show a markedly different behavior. Neither  $J_{sc}$  nor the FF deteriorate up to  $T_{\text{anneal}} > 170 \text{ °C}$  as a result of suppressed crystallization of the acceptor mixture and hence an unaltered blend nanostructure (Figure 7c,d,e). We note a slight drop in  $V_{oc}$  by 10%, which occurs for the two binary blend devices as well as the ternary devices and may result from an adverse effect of annealing on the ZnO bottom interlayer.<sup>[38,39]</sup> Overall, the ternary blend devices display superior thermal stability as compared to the two binary blend ones, with a stable PCE up to 170 °C by maintaining the same blend nanostructure, which indicates that device fabrication and operation at very high temperatures can be considered.

In a final set of experiments, we studied the thermal stability during longer annealing times of up to 205 h. Binary and ternary devices were annealed at  $T_{\text{anneal}} = 130 \text{ °C}$  under dark and inert conditions. We chose this temperature to ensure that our annealing protocol does not affect the ZnO interface layer. Binary devices display a notable burn-in during the first 50 h, leading to a drop in PCE by at least one third (Figure 8). Strikingly, the addition of third component arrested the burn-in and resulted in a steady PCE in case of ternary devices, which we assign to a more stable nanostructure. The constant photovoltaic performance of ternary devices at 130 °C confirms that the use of an acceptor mixture is a powerful tool to improve the thermal stability of organic solar cells.

### 3. Conclusions

In this study, we have investigated the phase behavior of a binary non-fullerene acceptor mixture, ITIC-4F:ITIC-4Cl, which can undergo co-crystallization. Addition of the donor polymer PTB7-Th results in a ternary blend with a high  $T_g \approx 200$  °C. The acceptor mixture phase separates into tens of nanometer-sized domains, intertwined with polymer-rich domains, which effectively suppresses co-crystallization. The resulting non-crystalline ternary blend nanostructure remains unaltered despite annealing at temperatures up to 170 °C, resulting in stable photovoltaic devices. We conclude that the use of ternary blends facilitates fabrication protocols that expose the active layer to a high thermal stress. The combination of a high  $T_g$  and suppressed crystallization guarantees a highly reproducible and thermally robust nanostructure, which is of urgent need for upscaling of organic solar cells.

### 4. Experimental Section

**Materials:** PTB7-Th (number-average molecular weight  $M_n \approx 19$  kg mol<sup>-1</sup>, polydispersity index PDI = 4.4), ITIC-4F, and ITIC-4Cl were purchased from 1-Materials Inc. and used as received. Chlorobenzene was obtained from Sigma-Aldrich and used as received. All samples were processed from 20 g L<sup>-1</sup> chlorobenzene solutions. For more information, refer to device fabrication.

**Differential Scanning Calorimetry:** Measurements were done with a DSC2 from Mettler Toledo equipped with a Gas controller GC 200 system at a heating/cooling rate of 10 °C min<sup>-1</sup>. Samples were prepared by drop casting 4 mg of material on a glass slide, followed by transfer to a 40 µL Al crucible.

**Fast Scanning Calorimetry:** Measurements were done with a Flash DSC 1 from Mettler Toledo. A thin film was spin-coated directly on the backside of the sensor. The sample was first heated to 450 °C, followed by aging at different temperatures (60–225 °C) for 30 min; heating/cooling rate 4000 K s<sup>-1</sup> (see Figure 2a).

**Dynamic Mechanical Analysis:** Measurements were done with a Q800 from TA Instruments from room temperature to 300 °C at a frequency of 1 Hz and a heating rate of 3 °C min<sup>-1</sup>.<sup>[20,34]</sup> 2.5 cm × 0.5 cm pieces of a plain weave glass fiber mesh with a weight of 25 g m<sup>-2</sup> (Easycomposites) were cut at an angle of 45°, drop coated, and dried under vacuum at 60 °C for 60 min.

**Indirect Nanoplasmonic Sensing:** Details about the measurement and setup can be found in refs. [20,35].

**Grazing-Incident Wide-Angle X-Ray Scattering:** GIWAXS experiments were conducted on CMS beamline at NSLS II, Brookhaven National Lab. An X-ray of energy of 13.5 keV was directed onto the thin films at an incident angle of 0.15°. The generated diffractograms were collected by a Pilatus 1M detector placed 255 mm away from the sample along the incident X-ray beam.

**Polarized Optical Microscopy:** Images of samples on silicon wafers were taken with a Zeiss Axio Scope A1 optical microscope in cross-polarization and reflection mode.

**Scanning Electron Microscopy:** Imaging was done with a Leo Ultra 55 SEM at 3 kV using a secondary-electron detector at a working distance of  $\approx 10$  mm.

**Atomic Force Microscopy-Infrared Spectroscopy:** For local IR characterization, AFM-IR was used. Samples were spin-coated on oxygen plasma cleaned Si-wafers. AFM-IR measurements were performed in Tapping Mode with a Bruker/Anasys Instruments nanoIR3 (France/USA), equipped with an MIR-cat QT 2400 QCL laser from Daylight Solutions (USA). Gold-coated silicon tips were used: PR-EX-TnIR-A (75 kHz, 1–7 N m<sup>-1</sup>).

**Variable-Temperature Photoluminescence Spectroscopy:** Thin films were spin-coated on glass substrates coated with 90 nm Al, placed on a hot plate at ambient atmosphere, and excited with a green laser with peak emission at 530 nm (the spot size was narrowed with a 1 mm aperture). Emission spectra were recorded via an optical fiber from Ocean Optics (diameter 600 µm) with an Ocean Optics QE-Pro spectrometer in kinetic mode and 100 ms integration time during heating at 10 °C min<sup>-1</sup> from 30 to 260 °C.

**Photoluminescence, Raman and Photocurrent Phase Diagram:** The detailed sample description can be found in ref. [36]. While extracting the current the samples were scanned under a microscope (WITec alpha 300 RA confocal Raman setup). White photocurrent maps were extracted using the setup built-in white light, while excitation at 488 and 633 nm was used to measure the Raman and photoluminescence spectra at each position, respectively. The ternary composition diagram was constructed from the Raman fingerprints of the neat materials as well as the cross-section, refractive index, and extinction coefficient at 488 nm. All measurements were done co-locally to mitigate the spatial dependence.

**Device Fabrication:** Pre-patterned indium tin oxide (ITO) glass substrates were cleaned in an ultrasonic bath with acetone and isopropyl alcohol, dried under nitrogen flow, and treated with oxygen plasma. 20 mg ml<sup>-1</sup> of each of PTB7-Th, ITIC-4F, and ITIC-4Cl were dissolved in chlorobenzene overnight at 80 °C. The appropriate ratios of each were stirred for couple of hours before spin coating the active layer. No additives were added to evade any possible additive-induced crystallization in the active layer. A ZnO NP interlayer was deposited by spin coating a nanoparticle suspension from Avantama Inc. at 4000 rpm for 40 s, followed by annealing for 10 min at 80 °C in air. Active layers were spin-coated at 2000 rpm inside a glove box, followed by annealing as indicated. Finally, 10 nm MoO<sub>x</sub> followed by 100 nm silver were thermally evaporated at  $1 \times 10^{-6}$  bar. *I*–*V* curves were measured using Keithley 2400 source meter and a WaveLabs sinus-70 solar simulator calibrated to 1 sun, AM1.5 G.

**Thermal Stability of Devices:** All thermal stability experiments were conducted inside a glove box. The partial device stack (ITO/ZnO NP/Active layer) was annealed at different temperatures and for different times. The device fabrication was completed by evaporating MoO<sub>x</sub> and Ag as mentioned above. The devices were measured under a WaveLabs sinus-70 solar simulator calibrated to 1 sun, AM1.5 G.

### Supporting Information

Supporting Information is available from the Wiley Online Library or from the author.

### Acknowledgements

S.H. and S.H.K.P. contributed equally to this work. The authors acknowledge the King Abdullah University of Science and Technology (KAUST) Office of Sponsored Research (OSR) under OSR-2018-CPF-4106 and the Knut and Alice Wallenberg Foundation through the project “Mastering Morphology for Solution-borne Electronics” (2016.0059) for funding. M.C.-Q. and A.H. acknowledge the European Research Council (ERC) for funding under grant agreement no. 648901. The authors thank MCIU for a Ramón y Cajal contract, Ikerbasque Foundation for the Fellow program (J.M.) and grants Ref. PGC2018-094620-A-I00, SEV-2015-0496 and PGC2018-095411-B-I00. L.Y. thanks the National Nature Science Foundation of China (NSFC 21905185) for financial support. The authors thank the National Synchrotron Light Source II, Brookhaven National Lab (Suffolk, Upton, New York, USA) for beamtime.

### Conflict of Interest

The authors declare no conflict of interest.

## Keywords

co-crystals, glass transition temperatures, non-fullerene acceptors, suppressed crystallization, ternary solar cells

Received: June 29, 2020  
Revised: September 23, 2020  
Published online:

- [1] Y. Cui, H. Yao, J. Zhang, K. Xian, T. Zhang, L. Hong, Y. Wang, Y. Xu, K. Ma, C. An, C. He, Z. Wei, F. Gao, J. Hou, *Adv. Mater.* **2020**, 32, 1908205.
- [2] N. Gasparini, S. H. K. Paleti, J. Bertrandie, G. Cai, G. Zhang, A. Wadsworth, X. Lu, H.-L. Yip, I. McCulloch, D. Baran, *ACS Energy Lett.* **2020**, 5, 1371.
- [3] Y. Jiang, L. Sun, F. Jiang, C. Xie, L. Hu, X. Dong, F. Qin, T. Liu, L. Hu, X. Jiang, Y. Zhou, *Mater. Horiz.* **2019**, 6, 1438.
- [4] I. T. Sachs-Quintana, T. Heumüller, W. R. Mateker, D. E. Orozco, R. Cheacharoen, S. Sweetnam, C. J. Brabec, M. D. McGehee, *Adv. Funct. Mater.* **2014**, 24, 3978.
- [5] M. Schubert, B. A. Collins, H. Mangold, I. A. Howard, W. Schindler, K. Vandewal, S. Roland, J. Behrends, F. Krafft, R. Steyrleuthner, Z. Chen, K. Fostiropoulos, R. Bittl, A. Salleo, A. Facchetti, F. Laquai, H. W. Ade, D. Neher, *Adv. Funct. Mater.* **2014**, 24, 4068.
- [6] A. Zusan, K. Vandewal, B. Allendorf, N. H. Hansen, J. Pflaum, A. Salleo, V. Dyakonov, C. Deibel, *Adv. Energy Mater.* **2014**, 4, 1400922.
- [7] S. A. Mollinger, B. A. Krajina, R. Noriega, A. Salleo, A. J. Spakowitz, *ACS Macro Lett.* **2015**, 4, 708.
- [8] C. Müller, *Chem. Mater.* **2015**, 27, 2740.
- [9] S. Bertho, G. Janssen, T. J. Cleij, B. Conings, W. Moons, A. Gadisa, J. D'Haen, E. Goovaerts, L. Lutsen, J. Manca, D. Vanderzande, *Sol. Energy Mater. Sol. Cells* **2008**, 92, 753.
- [10] C. Lindqvist, A. Sanz-Velasco, E. Wang, O. Bäcke, S. Gustafsson, E. Olsson, M. R. Andersson, C. Müller, *J. Mater. Chem. A* **2013**, 1, 7174.
- [11] D. Angmo, M. Bjerring, N. C. Nielsen, B. C. Thompson, F. C. Krebs, *J. Mater. Chem. C* **2015**, 3, 5541.
- [12] A. Diaz de Zerio Mendaza, A. Melianas, S. Rossbauer, O. Bäcke, L. Nordstierna, P. Erhart, E. Olsson, T. D. Anthopoulos, O. Inganäs, C. Müller, *Adv. Mater.* **2015**, 27, 7325.
- [13] P. Cheng, C. Yan, Y. Wu, J. Wang, M. Qin, Q. An, J. Cao, L. Huo, F. Zhang, L. Ding, Y. Sun, W. Ma, X. Zhan, *Adv. Mater.* **2016**, 28, 8021.
- [14] A. Diaz de Zerio, C. Müller, *Adv. Energy Mater.* **2018**, 8, 1702741.
- [15] J. Hou, O. Inganäs, R. H. Friend, F. Gao, *Nat. Mater.* **2018**, 17, 119.
- [16] C. Yan, S. Barlow, Z. Wang, H. Yan, A. K. Y. Jen, S. R. Marder, X. Zhan, *Nat. Rev. Mater.* **2018**, 3, 18003.
- [17] A. Wadsworth, M. Moser, A. Marks, M. S. Little, N. Gasparini, C. J. Brabec, D. Baran, I. McCulloch, *Chem. Soc. Rev.* **2019**, 48, 1596.
- [18] J. Xin, X. Meng, X. Xu, Q. Zhu, H. B. Naveed, W. Ma, *Matter* **2019**, 1, 1316.
- [19] Q. Liang, J. Han, C. Song, X. Yu, D.-M. Smilgies, K. Zhao, J. Liu, Y. Han, *J. Mater. Chem. A* **2018**, 6, 15610.
- [20] L. Yu, D. Qian, S. Marina, F. A. A. Nugroho, A. Sharma, S. Hultmark, A. I. Hofmann, R. Kroon, J. Benduhn, D.-M. Smilgies, K. Vandewal, M. R. Andersson, C. Langhammer, J. Martín, F. Gao, C. Müller, *ACS Appl. Mater. Interfaces* **2019**, 11, 21766.
- [21] Z. Fei, F. D. Eisner, X. Jiao, M. Azzouzi, J. A. Röhr, Y. Han, M. Shahid, A. S. R. Chesman, C. D. Easton, C. R. McNeill, T. D. Anthopoulos, J. Nelson, M. Heeney, *Adv. Mater.* **2018**, 30, 1705209.
- [22] S. M. Swick, T. Gebraad, L. Jones, B. Fu, T. J. Aldrich, K. L. Kohlstedt, G. C. Schatz, A. Facchetti, T. J. Marks, *ChemPhysChem* **2019**, 20, 2608.
- [23] W. Köntges, P. Perkhun, J. Kammerer, R. Alkarsifi, U. Würfel, O. Margeat, C. Videlot-Ackermann, J.-J. Simon, R. R. Schröder, J. Ackermann, M. Pfannmöller, *Energy Environ. Sci.* **2020**, 13, 1259.
- [24] M. Jørgensen, K. Norrman, S. A. Gevorgyan, T. Tromholt, B. Andreasen, F. C. Krebs, *Adv. Mater.* **2012**, 24, 580.
- [25] F. C. Krebs, *Sol. Energy Mater. Sol. Cells* **2009**, 93, 394.
- [26] S. Strohm, F. Machui, S. Langner, P. Kubis, N. Gasparini, M. Salvador, I. McCulloch, H. J. Egelhaaf, C. J. Brabec, *Energy Environ. Sci.* **2018**, 11, 2225.
- [27] E. Bihar, D. Corzo, T. C. Hidalgo, D. Rosas-Villalva, K. N. Salama, S. Inal, D. Baran, *Adv. Mater. Technol.* **2020**, 5, 2000226.
- [28] C.-Y. Liao, Y. Chen, C.-C. Lee, G. Wang, N.-W. Teng, C.-H. Lee, W.-L. Li, Y.-K. Chen, C.-H. Li, H.-L. Ho, P. H.-S. Tan, B. Wang, Y.-C. Huang, R. M. Young, M. R. Wasielewski, T. J. Marks, Y.-M. Chang, A. Facchetti, *Joule* **2020**, 4, 189.
- [29] N. Gasparini, A. Salleo, I. McCulloch, D. Baran, *Nat. Rev. Mater.* **2019**, 4, 229.
- [30] G. R. Desiraju, R. Parthasarathy, *J. Am. Chem. Soc.* **1989**, 111, 8725.
- [31] V. R. Hathwar, T. N. G. Row, *Cryst. Growth Des.* **2011**, 11, 1338.
- [32] X. Song, N. Gasparini, L. Ye, H. Yao, J. Hou, H. Ade, D. Baran, *ACS Energy Lett.* **2018**, 3, 669.
- [33] J. Martín, N. Stingelin, D. Cangialosi, *J. Phys. Chem. Lett.* **2018**, 9, 990.
- [34] A. Sharma, X. Pan, J. A. Campbell, M. R. Andersson, D. A. Lewis, *Macromolecules* **2017**, 50, 3347.
- [35] F. A. A. Nugroho, A. Diaz de Zerio Mendaza, C. Lindqvist, T. J. Antosiewicz, C. Müller, C. Langhammer, *Anal. Chem.* **2017**, 89, 2575.
- [36] A. Harillo-Baños, X. Rodríguez-Martínez, M. Campoy-Quiles, *Adv. Energy Mater.* **2020**, 10, 2070001.
- [37] X. Rodríguez-Martínez, M. S. Vezie, X. Shi, I. McCulloch, J. Nelson, A. R. Goñi, M. Campoy-Quiles, *J. Mater. Chem. C* **2017**, 5, 7270.
- [38] A. Sharma, S. E. Watkins, G. Andersson, D. A. Lewis, *Energy Technol.* **2014**, 2, 462.
- [39] C. Jiang, R. R. Lunt, P. M. Duxbury, P. P. Zhang, *RSC Adv.* **2014**, 4, 3604.